water

MDPI

Article

Response of Streamflow to Future Land Use and Cover Change and Climate Change in the Source Region of the Yellow River

Hao Zhan [1], Jiang Zhang [2], Le Wang [1], Dongxue Yu [1], Min Xu [3] and Qiuan Zhu [3,*]

[1] College of Hydrology and Water Resources, Hohai University, Nanjing 210098, China; zhanhao@hhu.edu.cn (H.Z.); wangle2020@hhu.edu.cn (L.W.); dxyu0101@163.com (D.Y.)
[2] Institute of Geographic Sciences and Natural Resources Research, Chinese Academy of Sciences, Beijing 100101, China; zhangjiang@igsnrr.ac.cn
[3] College of Geography and Remote Sensing, Hohai University, Nanjing 210098, China; 211301060012@hhu.edu.cn
* Correspondence: zhuq@hhu.edu.cn

Abstract: This study utilizes meteorological and leaf area index (LAI) data for three shared socioeconomic pathways (SSP1–2.6, SSP2–4.5, and SSP5–8.5) from four general circulation models (GCMs) of the sixth climate model intercomparison project (CMIP6) spanning from 2015 to 2099. Employing calibrated data and incorporating future land use data under three SSPs, the distributed hydrology soil vegetation model (DHSVM) is employed to simulate streamflow in the source region of the Yellow River (SRYR). The research aims to elucidate variations in streamflow across different future scenarios and to estimate extreme streamflow events and temporal distribution changes under future land use and cover change (LUCC) and climate change scenarios. The main conclusions are as follows: The grassland status in the SRYR will significantly improve from 2020 to 2099, with noticeable increases in temperature, precipitation, and longwave radiation, alongside a pronounced decrease in wind speed. The probability of flooding events increases in the future, although the magnitude of the increase diminishes over time. Both LUCC and climate change contribute to an increase in the multi-year average streamflow in the region, with respective increments of 48.8%, 24.5%, and 18.9% under SSP1–2.6, SSP2–4.5, and SSP5–8.5. Notably, the fluctuation in streamflow is most pronounced under SSP5–8.5. In SSP1–2.6, the increase in streamflow during the near future (2020–2059) exceeds that of the distant future (2059–2099). Seasonal variations in streamflow intensify across most scenarios, leading to a more uneven distribution of streamflow throughout the year and an extension of the flood season.

Keywords: Yellow River; source region; CMIP6; climate change; flow; LAI

Citation: Zhan, H.; Zhang, J.; Wang, L.; Yu, D.; Xu, M.; Zhu, Q. Response of Streamflow to Future Land Use and Cover Change and Climate Change in the Source Region of the Yellow River. *Water* **2024**, *16*, 1332. https://doi.org/10.3390/w16101332

Academic Editor: Maria Mimikou

Received: 5 April 2024
Revised: 3 May 2024
Accepted: 5 May 2024
Published: 8 May 2024

1. Introduction

Water security is an integral component of national security, as it not only faces direct risks such as water-related disasters and engineering failures but also impacts economic security, food security, energy security, and ecological security. The Yellow River, according to its flow through provinces, accounts for over 30% of the total population and around 26% of the nation's gross domestic product (GDP). It is one of China's major ecological conservation areas and economic development zones [1]. In 2021, Zhengzhou experienced a record-breaking maximum hourly rainfall of 201.9 mm, surpassing the historical extreme value of hourly rainfall in mainland China [2]. As one of the world's most complex and challenging rivers, the ecological environment in the Yellow River basin remains fragile, posing a severe challenge to water resource security [3,4]. Serving as one of the vital runoff-producing areas in the Yellow River, the source region of the Yellow River (SRYR) contributes 35% of the total runoff of the Yellow River despite covering only around 16% of the basin's total area [5]. Therefore, changes in runoff in the SRYR can significantly affect the eco-hydrological processes in the middle and lower reaches of the Yellow River [6].

Analyzing the evolving characteristics of hydrological elements under changing environmental conditions is paramount for regional water resource planning and sustainable development. Climate change and human activities are the two primary drivers of environmental change [7,8]. Land use and cover change (LUCC) is a key indicator reflecting the impact of human activities on hydrological cycles [9], and changes in basin hydrological processes attributable to LUCC cannot be overlooked. The impacts of climate change and LUCC on hydrological processes vary due to significant regional differences [10]. In some regions, climate change has a more significant impact on hydrology than LUCC [11,12]. Furthermore, in areas characterized by urbanization, industrialization, or dominant agricultural practices, LUCC plays a more significant role in influencing hydrological processes [8,13–16]. Therefore, there is an urgent need to investigate the impacts of future LUCC and climate change on hydrology [17], providing valuable insights for water resource management authorities.

Due to the complexity of explaining the mechanisms underlying the impact of future environmental changes on streamflow through statistical analysis, current research on future streamflow mainly relies on hydrological models driven by future climate data for simulation. Several models have been used to predict future hydrological processes, including the SWAT model [18–21], the VIC model [22,23], the MIKE SHE model [24], and the Budyko model [25,26]. Compared to the Budyko model, hydrological models often require a large amount of forcing data. This confirmed the most critical restriction for the widespread use of distributed hydrological models: the need for more detailed data about all hydrological components [27], mainly when dealing with large spatial datasets. The VIC model can reflect changes in vegetation quality, and the significant differences between considering and not considering dynamic LAI display pronounced trends [28]. However, the SWAT and MIKE SHE models characterize LUCC in terms of land use type, which cannot consider changes in vegetation growth status [12,24]. Actually, the DHSVM can also consider changes in vegetation quality and has been widely used in hydrological simulations under climate change and LUCC. Therefore, this study utilizes the DHSVM to forecast future changes in streamflow, providing alternative reference values for hydrological simulations in the SRYR.

In previous studies related to the estimation of future streamflow changes in the SRYR, Wang [29] simulated the changes in streamflow using the SWAT model based on CMIP5 data for the period from 2011 to 2090. The results indicated a decrease in precipitation, an increase in temperature, and a decrease in streamflow. Ji et al. [30] constructed a SWAT model for the Yellow River basin using CMIP5 data. Their study showed that the average streamflow at the Tangnaihai hydrological station will increase from 2040 to 2060, with a decreasing trend in spring and an increasing trend in winter. Various studies have reached different conclusions regarding future streamflow trends, indicating the need for further quantitative analysis of the SRYR.

Meanwhile, research has shown that global models of the sixth climate model intercomparison project (CMIP6) can effectively reproduce the spatial distribution of temperature and precipitation in China [31]. The CMIP6 is the most extensive effort in terms of the number of general circulation models (GCMs), the design of scientific experiments, and the provision of simulation data initiated by the World Climate Research Programme (WCRP) [32]. The CMIP6 introduces new projection scenarios that are different from the CMIP5 RCP scenarios, referred to as the scenario model intercomparison project (ScenarioMIP). The ScenarioMIP combines different future representative concentration pathways (RCPs) with shared socioeconomic pathways (SSPs), making it easier to assess the costs and benefits of mitigation actions and filling gaps between typical pathways in the CMIP5 [33], thus providing more reasonable and reliable climate simulation results.

We selected three representative climate scenarios: SSP1–2.6, SSP2–4.5, and SSP5–8.5. SSP1–2.6 represents a shallow range of scenarios, which is an updated version of the RCP2.6 scenario. It combines low vulnerability, low mitigation pressure, and low radiative forcing. Under the sustainable development pathway SSP1–2.6, the radiative forcing

stabilizes at -2.6 W/m^2 by 2100. SSP2–4.5 represents a moderate forcing scenario, which is an updated version of the RCP4.5 scenario. It combines moderate societal vulnerability with moderate radiative forcing. Under the intermediate development pathway SSP2–4.5, the radiative forcing stabilizes at -4.5 W/m^2 by 2100. SSP5–8.5 represents a combination of high societal vulnerability and a high forcing level, which is an updated version of the RCP8.5 scenario. Under the conventional development pathway with high fossil fuel consumption, SSP5–8.5, the radiative forcing reaches 8.5 W/m^2 by 2100.

Most studies considering future changes in the upper Yellow River basin are limited to climate change [34,35] or focus solely on the changes in a particular meteorological element [36]. However, there have been studies in other regions that comprehensively consider both land use and cover change (LUCC) and climate change in future predictions [24,37–39]. Our research contributes to the study of the extremely scarce future hydrological processes in the SRYR [21,40]. Additionally, we comprehensively consider the impacts of LUCC and climate change on future streamflow. Not only do we consider the areas of land use types, but we also consider the leaf area index (LAI), which reflects vegetation quality, making our consideration of surface changes more comprehensive. Due to the use of different weighted combinations of multiple models that could potentially yield better simulation results [41–45], our study employs an arithmetic mean of multiple models for ensemble modeling based on the latest CMIP6 data. Furthermore, the future land use data under three SSPs was also used to improve simulation accuracy.

The results can provide a more comprehensive reference for watershed flood control, ecological governance, and economic development. The main scientific goals addressed in this paper are (1) to conduct an applicability assessment of the DHSVM in the SRYR; (2) to explore the trends of LUCC and climate change in the SRYR from 2020 to 2099; and (3) to analyze the changes in streamflow under different scenario combinations in different future periods.

2. Materials and Methods

2.1. Study Area

The source region of the Yellow River (SRYR) encompasses the area of the SRYR located above the Tangnaihai hydrological station (32°9′~36°2′ N, 95°59′~103°34′ E) in the northeastern portion of the Tibetan Plateau. Within the SRYR, there are twelve meteorological stations (Maduo, Dari, Gande, Jiuzhi, Hongyuan, Ruoergai, Maqu, Henan, Maqin, Zeku, Tongde, and Xinghai), as shown in Figure 1. The river length in the SRYR measures 1553 km, accounting for 28.4% of the total length of the Yellow River [46]. Encompassing 124,000 km^2, the source area exhibits elevations ranging from 2842 to 6226 m. The terrain is characterized by higher elevations in the west and south, transitioning to lower elevations in the east and north. The climate is classified as inland alpine humid or semi-humid, with temperatures ranging from -4 to 5 °C and daily averages exceeding 0 °C between May and September. Annual precipitation averages between 220 and 780 mm, with significant interannual variability; precipitation distribution throughout the year is uneven. Both temperature and precipitation exhibit a gradual decrease from southeast to northwest. Overall, the region typically encounters dry winters, spring droughts, and intense precipitation events during summer and autumn (June to September).

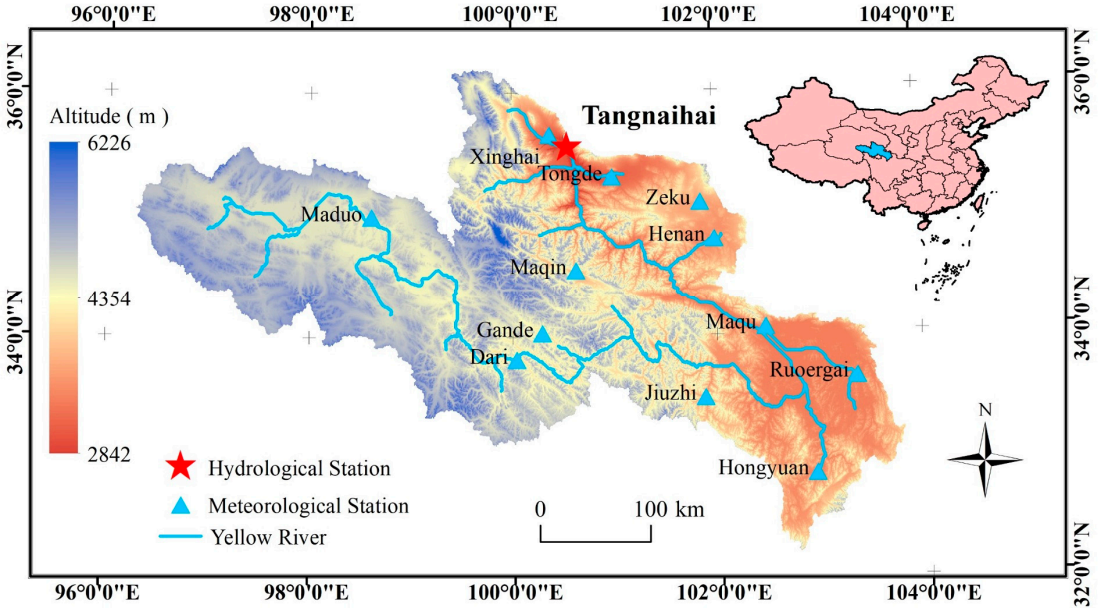

Figure 1. The study area. The inset shows the position of the study within the entire country.

2.2. Model and Data Preprocessing

The DEM data were obtained from the Resource and Environment Science and Data Center (https://www.resdc.cn/, accessed on 4 April 2024), specifically the provincial DEM 90m dataset (SRTM 90m). Soil-type data were sourced from the National Earth System Science Data Center. Model validation data were retrieved from the Hydrological Yearbook published by the Hydrological Bureau of the Ministry of Water Resources of the People's Republic of China, which includes daily average flow data from the Tangnaihai hydrological station (1981–2020).

The land use data from 1981 to 2020 originated from China's annual land use/cover datasets (CLUD-A) [47]. The leaf area index (LAI) data were acquired from the official website of the University of Maryland, USA, including AVHRR (1981–2018) (V50) and Modis_500m (2000–2021) datasets (http://www.glass.umd.edu/, accessed on 4 April 2024). Meteorological data from 1981 to 2020 were obtained from the daily climate dataset compiled by the National Meteorological Information Center of China. Because of the absence of longwave and shortwave radiation in historical meteorological data, based on data such as sunshine hours, average vapor pressure, and temperature, shortwave radiation was calculated using the methodology in the FAO study [48] and longwave radiation was calculated according to the Handbook of Hydrology [49].

Due to the superior performance of multi-model ensembles compared to individual models and the reduced simulation uncertainty [36], this study incorporates multiple general circulation model (GCM) datasets from the sixth climate model intercomparison project (CMIP6), which include all necessary meteorological and LAI data. As the DHSVM applied in the SRYR operates at a temporal resolution of 3 h, four GCMs were selected based on the precision of their temporal resolution, namely MPI-ESM1-2-LR, CMCC-CM2-SR5, CMCC-ESM2, and EC-Earth3-Veg, as detailed in Table 1.

Table 1. Description of the climate models used in the study.

GCM	Spatial Resolution	Experiment ID	Variant Label	Temporal Resolution						
				Relative Humidity	Precipitation	Longwave Radiation	Shortwave Radiation	Wind Speed	Air Temperature	LAI
MPI-ESM1-2-LR	192 × 96	ssp126, ssp245, ssp585	r1i1p1f1	6hrPlev	3 h	3 h	3 h	E3 h	3 h	Lmon
CMCC-CM2-SR5	288 × 192			day						
CMCC-ESM2	288 × 192			day						
EC-Earth3-Veg	512 × 256			day						

Due to the insufficient spatial resolution of the land use harmonization (LUH2) dataset at 0.25° × 0.25°, this study adopts the future LUCC data for China under the shared socioeconomic pathways (SSPs) scenarios from 2020 to 2099, as predicted by Liao et al. [50] based on the LUH2 dataset and the future land use simulation (FLUS) model (http://www.geosimulation.cn/China_PFT_SSP-RCP.html, accessed on 4 April 2024). This dataset is utilized to represent the vegetation area changes in the SRYR from 2020 to 2099 and to drive the DHSVM.

The overlapping period of the four GCMs spans from 2015 to 2099, with model data from 2015 to 2019 used for calibration. Subsequently, the period from 2020 to 2099, totaling 80 years, was selected as the study period. Climate scenarios were chosen to represent low, medium, and high forcings, denoted as SSP1–2.6, SSP2–4.5, and SSP5–8.5, respectively [33]. Meteorological elements include temperature, wind speed, humidity, shortwave radiation, longwave radiation, and precipitation, comprising six variables in total. The humidity data for the four models were subjected to linear interpolation using the cdo command to obtain humidity data at a 3 h interval. Meteorological and LAI data for the 12 meteorological stations depicted in Figure 1 were extracted for each GCM under different climate scenarios. The average values for each meteorological station were calculated to reduce GCM differences.

Based on the average data of the four GCMs for 2015–2019 and the average observed data from actual meteorological stations, a linear correction was applied to the average meteorological element data from the GCMs for 2020–2099 due to its simplicity and suitability [51,52]. For calibrating GCM data at a local scale, linear correction is more effective and efficient than statistical and dynamic scale corrections [53]. Linear scaling takes into account the difference between the mean correction value and the mean value of the observations to eliminate bias in the data. After eliminating the differences between the GCMs and historical data, meteorological element data for the 12 meteorological stations in the SRYR for 2020–2099 were obtained. LAI data were used to represent changes in vegetation growth status from 2020 to 2099. Monthly average LAI values for the 12 meteorological stations were calculated for each GCM, representing the LAI value for that GCM in the SRYR for that month. Subsequently, each month's average of the four GCMs was calculated to represent the vegetation growth status level in the SRYR. Similar correction operations were performed on the LAI data. The formula for linear calibration is as follows:

$$data^{*}GCM = dataGCM + \left(data^{-}OBS - data^{-}GCM\right) \quad (1)$$

where $data^{*}GCM$ represents the calibrated future monthly meteorological or LAI data; $dataGCM$ represents the uncalibrated future monthly meteorological or LAI data; $data^{-}OBS$ represents the average observed monthly meteorological or LAI data from 2015 to 2019; and $data^{-}GCM$ represents the uncalibrated average monthly meteorological or LAI data from the GCM from 2015 to 2019.

2.3. Model Calibration and Validation

The model parameters were calibrated based on studies conducted in environments similar to those in Northwestern China [54,55]. The model primarily focused on calibrating the following sensitive parameters: lateral and vertical saturated hydraulic conductivity, exponential decrease, porosity, minimum stomatal resistance, vegetation height, LAI, and vapor pressure deficit [56,57]. Research indicates that when grassland predominates as the primary surface vegetation type, greater attention should be given to the values of soil parameters [57]. Calibration was conducted using manual calibration methods. Initially, key sensitivity parameters were adjusted to align the simulated flow at the Tangnaihai station with the observed flow. Subsequently, parameters were iteratively adjusted based on control variables to achieve optimal simulation performance. We constrained the adjustment of each parameter within its known range or assumed range, ensuring that modifications were within reasonable bounds. The default model parameters sourced from

(https://www.pnnl.gov/sites/default/files/media/file/DHSVM%203.1.2_0.zip, accessed on 4 April 2024) and other parameters were modified during calibration in Table 2.

Table 2. Calibration of parameters in the DHSVM.

Parameter Name	Unit	Calibration Value
Snow roughness [1]	m	0.001
Snow threshold [2]	°C	−0.5
Rain LAI multiplier [2]	NA *	0.00005
Understory monthly LAI [3]	NA	LAI data
Height [3]	m	0.4
Field capacity (fraction) [1]	NA	0.23, 0.23, 0.23
Vertical conductivity [3]	m/s	4.3×10^{-5}, 4.3×10^{-5}, 4.3×10^{-5}
Number of days since last snow fall [3]	NA	210
Temperature of bottom (top) layer of snow pack [3]	°C	0
Temperature at soil surface [3]	°C	0
Soil temperature for each root zone layer [3]	°C	0
Volumetric soil moisture content for each layer [3]	°C	0.45, 0.45, 0.45

Notes: * NA, not applicable; [1] Origin is inferred from [55]; [2] Origin is inferred from [54]; [3] Calibrated.

The DHSVM's accuracy was predominantly assessed using the Nash–Sutcliffe Efficiency (NSE) [58]. Additional validation metrics employed to assess the DHSVM's performance include the coefficient of determination (R^2) and the ratio of Root Mean Square Error to the standard deviation of observations (RSR). These accuracy metrics are defined as follows:

The NSE is defined as:

$$\mathrm{NSE} = 1 - \left[\frac{\sum_{i=1}^{n} (Q_{obs,i} - Q_{sim,i})^2}{\sum_{i=1}^{n} (Q_{obs,i} - \overline{Q_{obs}})^2} \right] \quad (2)$$

The R^2 is defined as:

$$R^2 = \left[\frac{\sum_{i=1}^{n} (Q_{obs,i} - \overline{Q_{obs}})(Q_{sim,i} - \overline{Q_{sim}})}{\sqrt{\sum_{i=1}^{n} (Q_{obs,i} - \overline{Q_{obs}})^2} \sqrt{\sum_{i=1}^{n} (Q_{sim,i} - \overline{Q_{sim}})^2}} \right]^2 \quad (3)$$

The RSR is defined as:

$$\mathrm{RSR} = \frac{\sqrt{\sum_{i=1}^{n} (Q_{obs,i} - Q_{sim,i})^2}}{\sqrt{\sum_{i=1}^{n} (Q_{obs,i} - \overline{Q_{obs}})^2}} \quad (4)$$

where $Q_{\mathrm{obs},i}$, $Q_{sim,i}$, $\overline{Q_{\mathrm{obs}}}$, and $\overline{Q_{sim}}$ are the observed values, simulated values, mean of observed values, and mean of simulated values, respectively. n represents the total number of data points corresponding to the number of time increments over a given period.

The NSE assumes values range from $-\infty$ to 1, where the values close to one indicate better performance. The R^2 describes the proportion of the variance in measured data explained by the model, with values ranging from 0 to 1; higher values indicate less error variance. The RSR varies from the optimal value of 0 to a large positive value. Lower RSR values represent better model simulation performance.

2.4. Mann–Kendall Trend Test

We employed the Mann–Kendall trend test method to investigate further the statistical characteristics of environmental and flow changes in the SRYR. The Mann–Kendall test is a non-parametric method for testing the trend of time series data [59,60], recommended

by the World Meteorological Organization (WMO). The Mann–Kendall test can be used to examine whether data sequences exhibit monotonic trends, and it has essential applications in trend analysis in hydrological, meteorological, and other fields. For a time series x, the computing formula for the Mann–Kendall trend test statistic S is as follows:

$$S = \sum_{k=1}^{n-1} \sum_{j=k+1}^{n} \operatorname{sgn}(x_j - x_k) \tag{5}$$

where x_j represents the jth data value of the time series, n is the number of data points in the sequence, and sgn denotes the sign function, defined as the following:

$$\operatorname{sgn}(x_j - x_k) = \begin{cases} 1 & (x_j - x_k > 0) \\ 0 & (x_j - x_k = 0) \\ -1 & (x_j - x_k < 0) \end{cases} \tag{6}$$

A negative value of S indicates a decreasing trend in the data, while a positive value indicates an increasing trend. Assuming each variable is independently and identically distributed, the variance is calculated as follows:

$$\operatorname{Var}(S) = \frac{n(n-1)(2n+5)}{18} \tag{7}$$

The test statistic Z is calculated according to the following formula:

$$Z \begin{cases} \frac{S-1}{\sqrt{var(S)}} & (S > 0) \\ 0 & (S = 0) \\ \frac{S+1}{\sqrt{var(S)}} & (S < 0) \end{cases} \tag{8}$$

Absolute values of Z greater than 1.65, 1.96, and 2.58 indicate confidence intervals of 90%, 95%, and 99% or significance levels, p, less than 10%, 5%, and 1%, respectively [61]. Based on the magnitude of the p-value, trends can be classified to demonstrate their statistical significance. $p < 0.01$ indicates a highly significant trend, $0.01 < p < 0.05$ indicates a significant trend, and $p > 0.10$ indicates a trend that is not significant.

2.5. Scenario Setting

To investigate the hydrological response processes under climate change and LUCC in the future period of the SRYR, three types of change scenarios, namely S1, S2, and S3, were established, along with three climate scenarios, namely SSP1–2.6, SSP2–4.5, and SSP5–8.5. This resulted in nine scenario combinations, as shown in Table 3.

Table 3. Scenario setting for the SRYR from 2020 to 2099.

Scenario Combinations	Grassland Area Data	Leaf Area Index Data	Meteorological Data	Description
S1_SSP1–2.6	Predicted for 2020–2099	Predicted for 2020–2099	Predicted for 2020 under SSP1–2.6	To reflect hydrological responses of the SRYR to LUCC under SSP1–2.6, SSP2–4.5, and SSP5–8.5, respectively
S1_SSP2–4.5			Predicted for 2020 under SSP2–4.5	
S1_SSP5–8.5			Predicted for 2020 under SSP5–8.5	
S2_SSP1–2.6	Predicted for 2020	Predicted for 2020	Predicted for 2020–2099 under SSP1–2.6	To reflect hydrological responses of the SRYR to climate change under SSP1–2.6, SSP2–4.5, and SSP5–8.5, respectively
S2_SSP2–4.5			Predicted for 2020–2099 under SSP2–4.5	
S2_SSP5–8.5			Predicted for 2020–2099 under SSP5–8.5	

Table 3. *Cont.*

Scenario Combinations	Grassland Area Data	Leaf Area Index Data	Meteorological Data	Description
S3_SSP1–2.6	Predicted for 2020–2099	Predicted for 2020–2099	Predicted for 2020–2099 under SSP1–2.6	To reflect hydrological responses of the SRYR to LUCC and climate change under SSP1–2.6, SSP2–4.5, and SSP5–8.5, respectively
S3_SSP2–4.5			Predicted for 2020–2099 under SSP2–4.5	
S3_SSP5–8.5			Predicted for 2020–2099 under SSP5–8.5	

3. Results and Discussion

3.1. Validation and Adaptability Evaluation of DHSVM in the Source Region of the Yellow River (SRYR)

The study employed a temporal resolution of 3 h and a spatial resolution of 500 m. The calibration period was from 1 January 1981 to 31 December 2010 and the validation period was from 1 January 2011 to 31 December 2020. On a monthly scale, both the calibration period's NSE and R^2 exceed 0.84, while during the validation period, both NSE and R^2 are greater than 0.75. On a daily scale, both NSE and R^2 are above 0.79 during the calibration period, and both NSE and R^2 are greater than 0.72 during the validation period. The RSR stayed below 0.45 in calibration, while the maximum value was 0.51 in validation.

Daily and monthly validation indicators were high for both the calibration period from 1981 to 2010 and the validation period from 2011 to 2020, suggesting a reliable model for estimating streamflow. Monthly calibration and validation performance was better than daily calibration and validation, which is expected for hydrological models. Overall, Figure 2 shows that the model evaluation metrics of both the calibration and validation periods meet the accuracy requirements. The DHSVM can accurately depict the streamflow simulation in the source region of the Yellow River (SRYR), demonstrating good applicability (both the NSE and R^2 exceed 0.75 on a monthly scale). Its high simulation accuracy makes it suitable for streamflow estimation under future land use and cover change (LUCC) and climate change scenarios.

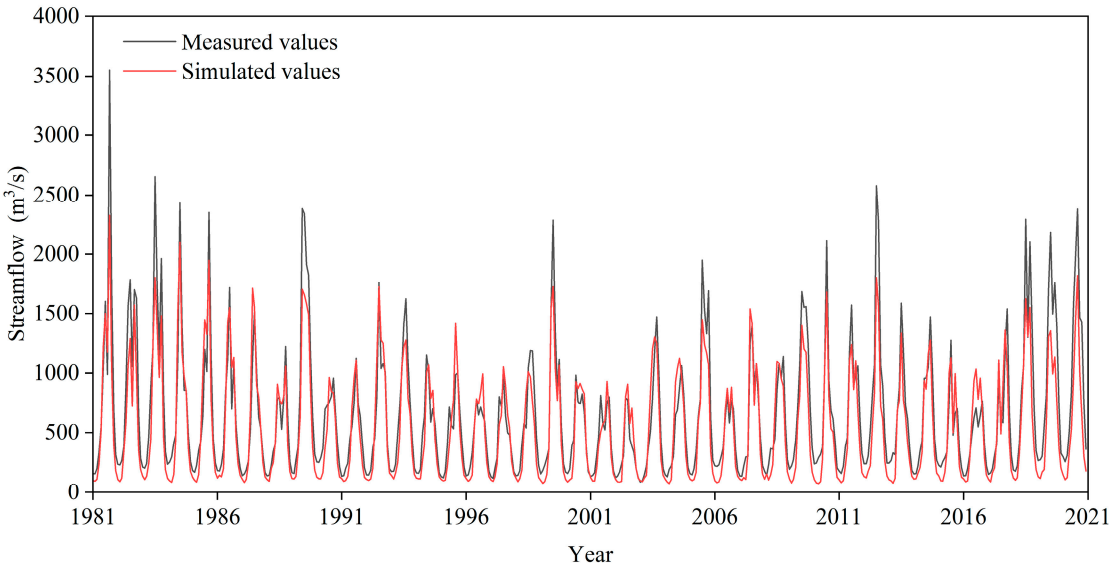

Figure 2. Comparison of observed and simulated monthly flow rates at the Tangnaihai station in the SRYR from 1981 to 2020.

3.2. Future Grassland and Climate Dynamics in the SRYR

Grassland is the primary land use type in the SRYR. Therefore, the yearly sequence of grassland growth status and the five-year sequence of grassland area changes in the SRYR from 2020 to 2099 were analyzed to discern future trends in grassland dynamics.

As depicted in Figure 3, the variation range of the grassland leaf area index (LAI), which represents the quality of grassland growth, is notably higher than that of grassland area under three climate scenarios, indicating that LAI governs grassland changes. Grassland LAI shows an increasing trend across all three climate scenarios, signifying an improvement in grassland growth status. Under SSP1–2.6, SSP2–4.5, and SSP5–8.5, LAI increased by 39%, 51%, and 72%, respectively. Conversely, the change in grassland area remains below 1% under all three climate scenarios, exhibiting a decreasing trend under SSP1–2.6 and a similar increasing trend under SSP2–4.5 and SSP5–8.5.

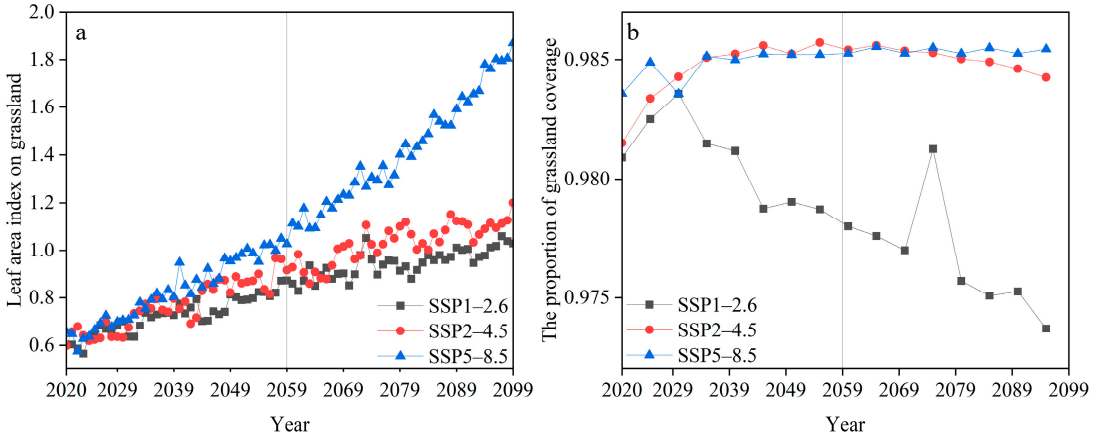

Figure 3. Grassland surface area and grassland growth in the SRYR, 2020–2099. (**a**) Growth on grasslands based on leaf area index. (**b**) The proportion of grassland coverage in the SRYR. The vertical lines in each plot mark the year 2059.

In summary, the grassland growth status in the SRYR from 2020 to 2099 markedly improves, indicating overall positive development in grassland quality and quantity.

We conducted statistical analysis on the yearly variation sequences of six meteorological elements in the SRYR from 2020 to 2099. Due to the abundance of data, we calculated the average values for different periods. Based on the division into recent future (2020–2059) and distant future (2059–2099) periods, we further subdivided the years from 2020 to 2099 into eight intervals. For instance, the years 2020–2029 were designated as the 2020s, and so forth, with 2090–2099 referred to as the 2090s. As illustrated in Figure 4, there is a notable increasing trend in temperature, precipitation, and longwave radiation, while wind speed exhibits a distinct decreasing trend in the future.

We calculated the relative change rates of each meteorological element between 2020 and 2099 compared to 2020, and temperature and precipitation demonstrate the highest fluctuations among all elements. Specifically, the temperature under SSP2–4.5 exhibits the largest Mann–Kendal Z-value (3.34) and a growth rate of 180%, indicating the most significant increase. Meanwhile, precipitation under SSP5–8.5 shows the largest Mann–Kendal Z-value (3.34) and a growth rate of 22%, indicating the highest increase. The change rates of other meteorological elements are all below 20%, as summarized in Table 4.

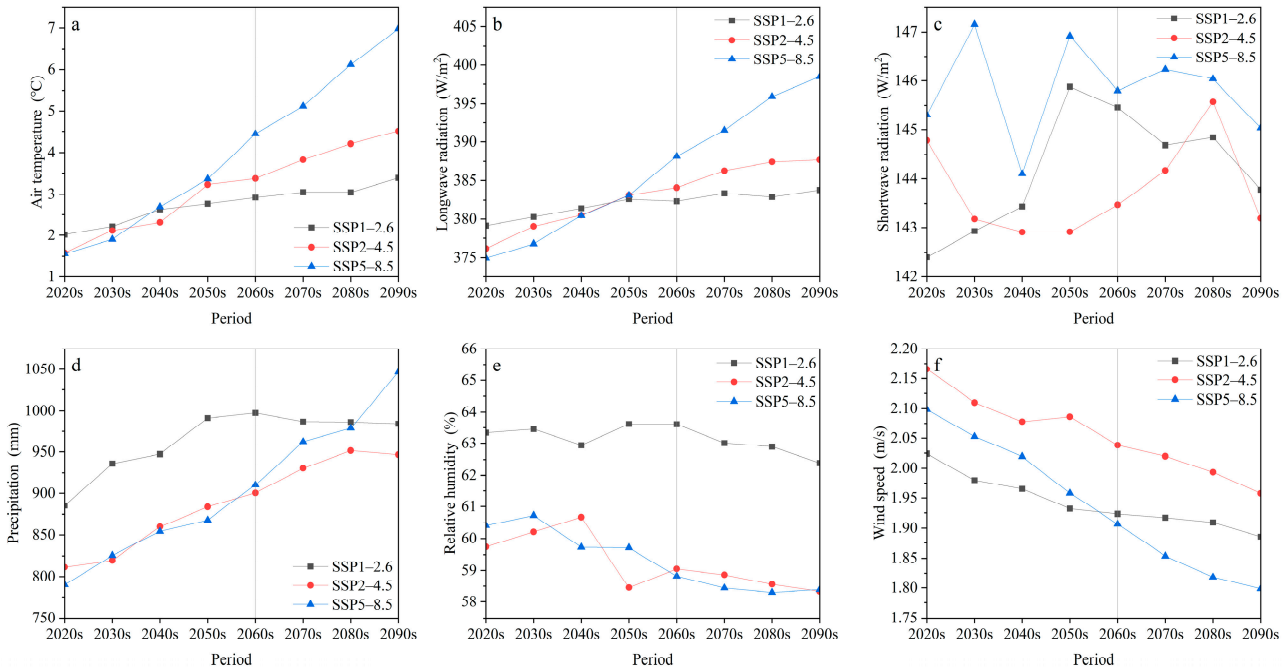

Figure 4. Average meteorological element change per decade for SRYR from 2020 to 2099. (**a**) Air temperature; (**b**) longwave radiation; (**c**) shortwave radiation; (**d**) precipitation; (**e**) relative humidity; (**f**) wind speed. The vertical lines in each plot mark the period 2060s.

Table 4. The statistical indicators of meteorological elements under various climate scenarios (the numbers under columns 3 (2020) and 4 (2020–2099) are mean values).

Meteorological Elements	Scenarios	2020	2020–2099	Change Rate	Mann–Kendal Z-Value	*p*
Air temperature (°C)	SSP1–2.6	1.9	2.8	44%	3.09	0.002
	SSP2–4.5	1.1	3.1	180%	3.34	0.0008
	SSP5–8.5	1.9	4.0	115%	3.34	0.0008
Longwave radiation (W/m^2)	SSP1–2.6	380.7	382.0	0%	2.85	0.004
	SSP2–4.5	373.9	383.1	2%	3.34	0.0008
	SSP5–8.5	372.0	386.2	4%	3.34	0.0008
Shortwave radiation (W/m^2)	SSP1–2.6	134.7	144.2	7%	1.11	0.27
	SSP2–4.5	149.1	143.8	−4%	0.62	0.54
	SSP5–8.5	149.2	145.8	−2%	−0.37	0.71
Precipitation (mm)	SSP1–2.6	920.7	964.4	5%	1.11	0.27
	SSP2–4.5	797.1	888.0	11%	3.09	0.002
	SSP5–8.5	739.3	904.5	22%	3.34	0.0008
Relative humidity (%)	SSP1–2.6	63.9	63.2	−1%	−1.36	0.17
	SSP2–4.5	60.1	59.2	−1%	−1.86	0.06
	SSP5–8.5	56.5	59.3	5%	−2.85	0.004
Wind speed (m/s)	SSP1–2.6	2.0	1.9	−1%	−3.34	0.0008
	SSP2–4.5	2.3	2.1	−10%	−3.09	0.002
	SSP5–8.5	2.2	1.9	−10%	−3.34	0.0008

3.3. Streamflow Analysis under Future LUCC (Land Use and Cover Change) and Climate Change

3.3.1. Analysis of Mean Flow, Change Rate, and Coefficient of Variation

We calculated the rate of change of the simulated annual average flow compared to historical results and the coefficient of variation by dividing the sample standard deviation by the sample mean and then multiplying by 100%. The annual mean flow, streamflow

change rate, and coefficient of variation for different scenarios (S1, S2, and S3) and three climate scenarios in the SRYR for 2020–2099 are tabulated in Table 5.

Table 5. Statistics for annual average flow, flow change rate, and coefficient of variation of different scenarios and paths in different periods in the SRYR in the future (column 11 (recent future) refers to the period from 2020 to 2059, while column 12 (distant future) refers to the period from 2059 to 2099).

Variable	Scenario Combinations	2020s	2030s	2040s	2050s	2060s	2070s	2080s	2090s	Recent Future	Distant Future	Future	Coefficient of Variation
Period average annual flow (m^3/s)	S1_SSP1–2.6	947.6	932.9	925.0	910.7	900.7	892.5	892.1	884.8	929.1	892.5	910.8	0.025
	S1_SSP2–4.5	738.8	724.8	714.8	701.5	696.5	681.2	675.4	671.7	720.0	681.2	700.6	0.035
	S1_SSP5–8.5	664.1	645.5	627.0	608.0	587.9	566.7	545.5	520.1	636.1	555.0	595.6	0.084
	S2_SSP1–2.6	912.4	981.3	988.7	1043.0	1053.1	1030.8	1042.7	1024.0	981.4	1037.7	1009.5	0.047
	S2_SSP2–4.5	777.6	777.7	826.7	854.0	871.9	912.4	927.6	915.3	809.0	906.8	857.9	0.070
	S2_SSP5–8.5	729.3	780.7	805.7	810.1	854.4	910.0	914.9	1022.2	781.4	925.4	853.4	0.109
	S3_SSP1–2.6	904.9	959.0	957.9	996.1	996.4	964.2	976.6	951.0	954.5	972.1	963.3	0.030
	S3_SSP2–4.5	771.5	756.2	794.3	805.3	815.4	836.0	844.3	825.4	781.8	830.3	806.1	0.038
	S3_SSP5–8.5	729.3	762.0	766.1	748.4	764.6	790.3	766.7	829.7	751.4	787.8	769.6	0.039
Flow change rate (%)	S1_SSP1–2.6	46.4	44.1	42.9	40.7	39.1	37.9	37.8	36.7	43.5	37.9	40.7	Null
	S1_SSP2–4.5	14.1	12.0	10.4	8.4	7.6	5.2	4.3	3.8	11.2	5.2	8.2	
	S1_SSP5–8.5	2.6	−0.3	−3.2	−6.1	−9.2	−12.5	−15.7	−19.7	−1.7	−14.3	−8.0	
	S2_SSP1–2.6	40.9	51.6	52.7	61.1	62.7	59.2	61.1	58.2	51.6	60.3	55.9	
	S2_SSP2–4.5	20.1	20.1	27.7	31.9	34.7	40.9	43.3	41.4	25.0	40.1	32.5	
	S2_SSP5–8.5	12.6	20.6	24.5	25.1	32.0	40.6	41.3	57.9	20.7	42.9	31.8	
	S3_SSP1–2.6	39.8	48.1	48.0	53.9	53.9	48.9	50.9	46.9	47.4	50.2	48.8	
	S3_SSP2–4.5	19.2	16.8	22.7	24.4	26.0	29.1	30.4	27.5	20.8	28.3	24.5	
	S3_SSP5–8.5	12.6	17.7	18.3	15.6	18.1	22.1	18.4	28.2	16.1	21.7	18.9	

Taking the historical period from 1981 to 2020 as the baseline period, the observed annual mean flow at the Tangnaihai hydrological station during this period was 647.4 m^3/s. As depicted in Figure 5, except for the S1_SSP5–8.5 scenario combination, where the annual mean flow decreases compared to the baseline period, all other scenario combinations show an increase in annual mean flow. Specifically, all combinations in the S1 scenario exhibit a decreasing trend in annual mean flow, while those in the S2 and S3 scenarios demonstrate a fluctuating increasing trend. Regarding the S3 scenario, which involves changes in both meteorological and land surface data, the results indicate an increasing trend in the probability of flood disasters occurring in the SRYR during the future period from 2020 to 2099. However, the magnitude of this increase shows a long-term declining trend.

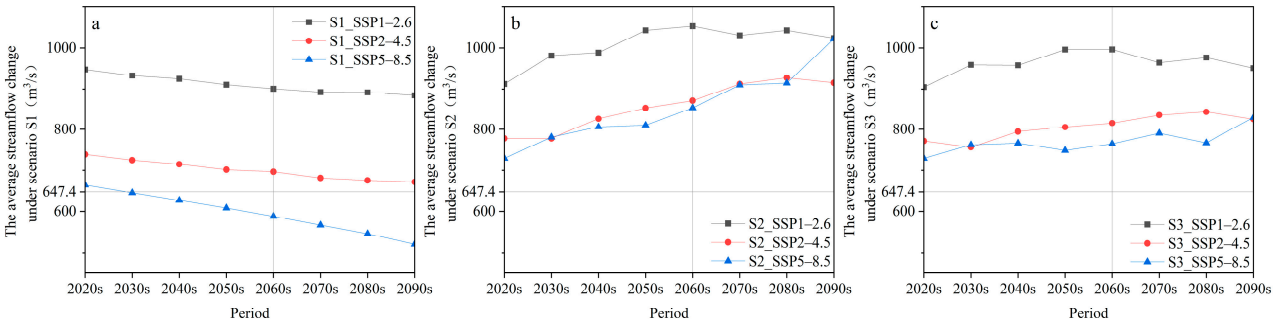

Figure 5. The average streamflow changes per decade from 2020 to 2099 in the three scenarios of S1, S2 and S3 in the SRYR. (**a**) Scenario S1. (**b**) Scenario S2. (**c**) Scenario S3.

In scenario S1, the annual average flow rate is 910.8 m^3/s at SSP1–2.6, with a coefficient of variation of 0.025 and Mann–Kendal Z-value of −3.34. At SSP2–4.5, the annual average flow rate is 700.6 m^3/s, with a co-efficient of variation of 0.035 and Mann–Kendal Z-value of −3.34. At SSP5–8.5, the annual average flow rate is 595.6 m^3/s, with a coefficient of variation of 0.084 and Mann–Kendal Z-value of −3.34. For scenario SSP1–2.6, the short-term rate of change is 43.5%, and the long-term rate of change is 37.9%. For scenario SSP2–4.5, the short-term rate of change is 11.2%, and the long-term rate of change is 5.2%. For scenario SSP5–8.5, the short-term rate of change is −1.7%, and the long-term rate of change is −14.3%.

In scenario S2, the annual average flow rate is 1009.5 m^3/s at SSP1–2.6, with a coefficient of variation of 0.047 and Mann–Kendal Z-value of 1.36. At SSP2–4.5, the annual average flow rate is 857.9 m^3/s, with a coefficient of variation of 0.070 and Mann–Kendal Z-value of 3.09. At SSP5–8.5, the annual average flow rate is 853.4 m^3/s, with a coefficient of variation of 0.109 and Mann–Kendal Z-value of 3.34. For scenario SSP1–2.6, the short-term rate of change is 51.6%, and the long-term rate of change is 60.3%. For scenario SSP2–4.5, the short-term rate of change is 25.0%, and the long-term rate of change is 40.1%. For scenario SSP5–8.5, the short-term rate of change is 20.7%, and the long-term rate of change is 42.9%.

In scenario S3, the annual average flow rate is 963.3 m^3/s at SSP1–2.6, with a coefficient of variation of 0.030 and Mann–Kendal Z-value of 0.62. At SSP2–4.5, the annual average flow rate is 806.1 m^3/s, with a coefficient of variation of 0.038 and Mann–Kendal Z-value of 2.60. At SSP5–8.5, the annual average flow rate is 769.6 m^3/s, with a coefficient of variation of 0.039 and Mann–Kendal Z-value of 2.35. For scenario SSP1–2.6, the short-term rate of change is 47.4%, and the long-term rate of change is 50.2%. For scenario SSP2–4.5, the short-term rate of change is 20.8%, and the long-term rate of change is 28.3%. For scenario SSP5–8.5, the short-term rate of change is 16.1%, and the long-term rate of change is 21.7%.

Scenario S1 shows the minimum rate of streamflow variation in the 2090s, while the maximum variation occurs during the 2020s. This indicates that scenario S1 has a relatively moderate degree of change in the 2090s and a more severe degree of change during the 2020s. Scenarios S2 and S3 show the minimum rate of streamflow variation during the 2020s, and the maximum variation occurs in the distant future. This suggests that scenarios S2 and S3 have a relatively moderate degree of change during the 2020s and a more severe degree of change in the distant future. Overall, LUCC and climate change are leading to an increase in the multi-year average streamflow in the SRYR from 2020 to 2099, with an increase of 48.8%, 24.5%, and 18.9%, under SSP1–2.6, SSP2–4.5, and SSP5–8.5, respectively. The coefficient of variation is the minimum under SSP1–2.6, suggesting relatively smooth fluctuations in future streamflow trends. The coefficient of variation is the maximum under SSP5–8.5, indicating more severe fluctuations in future streamflow trends, which is unfavorable for the sustainable use of water resources in the middle and lower reaches of the Yellow River.

In scenario S3, the increase in the annual average flow rate is the lowest under SSP5–8.5 for both the short-term (2020–2059) and long-term (2059–2099) periods and the highest under SSP1–2.6. Additionally, the annual average flow rate in the short term is lower than in the long term. These results indicate that under SSP1–2.6, the intensity of flood disasters is the highest in the SRYR from 2020 to 2099, while under SSP5–8.5, the intensity of flood disasters is the lowest and the streamflow trend is the most volatile. Furthermore, the increase in flow rate in the short term (2020–2059) is smaller than in the long term (2059–2099), and the variation in streamflow is more severe in the long term.

Scenario S3, compared to scenario S1 with climate data from 2020, exhibits warmer and wetter climatic conditions, resulting in higher flow rates. Similarly, compared to scenario S2 with land use data from 2020, scenario S3 demonstrates improved grassland conditions, leading to reduced flow rates. The warming and moistening trend in the SRYR from 2020 to 2099 not only increases basin flow but may also contribute to the significant improvement in grassland growth status (Mann–Kendal Z-values for SSP1–2.6, SSP2–4.5, and SSP5–8.5 are 11.09, 10.83, and 12.48, respectively). Comparing future climate change with simulated streamflow conditions, we found that precipitation is the highest under the SSP1–2.6 scenario, which may lead to the highest intensity of flood occurrence in the future (flow values for SSP1–2.6, SSP2–4.5, and SSP5–8.5 under scenario S1 are the highest) [62]. Conversely, the temperature is the highest under the SSP5–8.5 scenario and exhibits a significant increase (Mann–Kendal Z-value is 3.34), which may result in the most significant changes in streamflow in the future period (coefficients of variation for scenarios S1, S2, and S3 are the highest) [63].

3.3.2. Analysis of Extreme Monthly Average Flows

The extreme monthly flow values were calculated for the three climate scenarios in the SRYR for 2020–2099 under scenarios S1, S2, and S3. Although the years in which the maximum monthly flows occur differ for each scenario, they all occur between 2022 and 2049, while the minimum values occur between 2061 and 2099. Therefore, the LUCC and climate change fluctuations during this period deserve further research to enhance resistance to extreme events.

Under scenario S1 in SSP1–2.6, there are 80 months with extremely high monthly average flows exceeding 2000 m^3/s between 2020 and 2099, with the maximum flow occurring in June 2022 at 2288.1 m^3/s. This value represents the maximum flow that may occur among the three climate scenarios simulated during 2020–2099. The minimum monthly average flow occurs in January 2095 at 185.9 m^3/s. Under SSP2–4.5, no extremely high monthly average flows exceeding 2000 m^3/s were observed between 2020 and 2099. The maximum monthly flow occurs in September 2030 at 1535.8 m^3/s, with the minimum monthly flow occurring in January 2020 at 169.0 m^3/s. Under SSP5–8.5, no extremely high monthly average flows exceeding 2000 m^3/s were observed between 2020 and 2099. The maximum monthly flow occurs in June 2022 at 1477.9 m^3/s, while the minimum monthly flow occurs in December 2099 at 142.7 m^3/s. This value represents the minimum flow that may occur among the three climate scenarios simulated during 2020–2099.

Under scenario S2 in SSP1–2.6, there were 75 months with extremely high monthly average flows exceeding 2000 m^3/s between 2020 and 2099. The maximum monthly flow occurs in June 2049 at 2692.8 m^3/s. This value represents the maximum flow that may occur among the three climate scenarios simulated during 2020–2099. The minimum monthly average flow occurs in January 2026 at 159.3 m^3/s. Under SSP2–4.5, there were 12 months with extremely high monthly average flows exceeding 2000 m^3/s between 2020 and 2099. The maximum monthly flow occurs in June 2062 at 2220.5 m^3/s. The minimum monthly average flow occurs in February 2061 at 139.5 m^3/s. This value represents the minimum flow that may occur among the three climate scenarios simulated during 2020–2099. Under SSP5–8.5, there was one month with an extremely high monthly average flow exceeding 2000 m^3/s between 2020 and 2099. The maximum monthly flow occurs in June 2094 at 2056.0 m^3/s. The minimum monthly average flow occurs in February 2040 at 156.0 m^3/s.

Under scenario S3 in SSP1–2.6, there were 48 months with extremely high monthly average flows exceeding 2000 m^3/s between 2020 and 2099. The maximum monthly flow occurs in June 2049 at 2612.4 m^3/s. This value represents the maximum flow that may occur among the three climate scenarios simulated during 2020–2099. The minimum monthly average flow occurs in January 2026 at 159.3 m^3/s. Under SSP2–4.5, there were 5 months with extremely high monthly average flows exceeding 2000 m^3/s between 2020 and 2099. The maximum monthly flow occurs in July 2037 at 2147.8 m^3/s. The minimum monthly average flow occurs in February 2061 at 139.5 m^3/s. This value also represents the minimum flow that may occur among the three climate scenarios simulated during 2020–2099. It is necessary to prepare corresponding response strategies before extreme values occur. Under SSP5–8.5, there were 4 months with extremely high monthly average flows exceeding 2000 m^3/s between 2020 and 2099. The maximum monthly flow occurs in June 2038 at 2269.9 m^3/s. The minimum monthly average flow occurs in February 2040 at 156.0 m^3/s.

In all (S1, S2, and S3) categories, precipitation under SSP1–2.6 consistently remains the highest, which may result in the maximum flow rate always being associated with SSP1–2.6. The minimum flow values for S2 and S3 occurred under SSP2–4.5, which may be associated with the optimal vegetation growth conditions observed under SSP5–8.5.

3.3.3. Analysis of Changes in Monthly Average Flow Distribution

The annual average monthly flow of observed flow for the historical period from 1981 to 2020 is calculated. The multi-year average monthly flow for the three scenarios (S1, S2, and S3) from 2020 to 2099 is plotted, as shown in Figure 6.

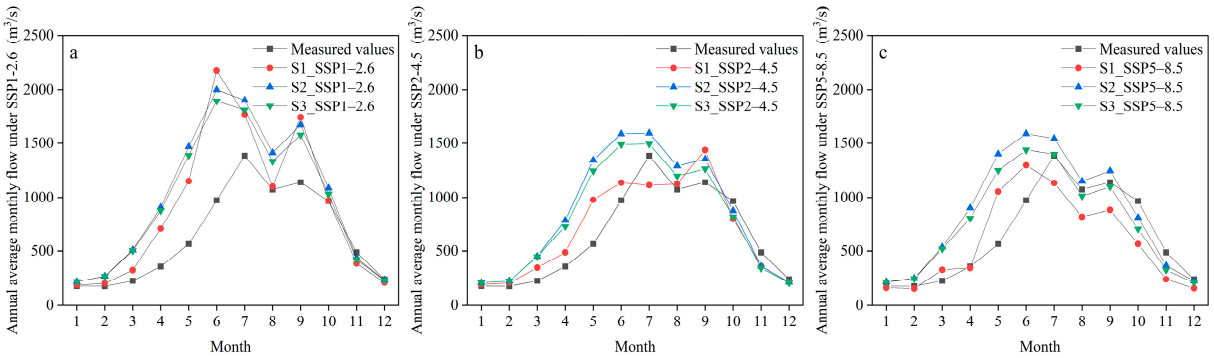

Figure 6. The intra-annual flow distribution for scenarios S1, S2, and S3 under three climate scenarios from 2020 to 2099. (**a**) SSP1–2.6; (**b**) SSP2–4.5; (**c**) SSP5–8.5.

Under the SSP1–2.6 climate scenario, all three scenarios (S1, S2, and S3) show an increase in flow compared to the historical period from January to October and a decrease from November to December. The Mann–Kendal Z-values for the flow in months January through June are all 2.63 for scenarios S1, S2, and S3. However, for scenario S2, the flow exhibits the highest relative increase compared to historical periods, with a growth of 61%. Scenario S2 shows the most significant increase, with the most pronounced increase observed in May, where the flow surged by 160% compared to historical periods. Scenario S3 shows the largest changes in April and November, with a 147% increase compared to the historical period in April and a 14% decrease in November.

Under the SSP2–4.5 climate scenario, except for the flow in July for scenario S1, all three scenarios (S1, S2, and S3) show an increase in flow from January to September compared to the historical period. From October to December, there is a decrease in flow compared to the historical period, with a decrease in flow during the autumn season and an increase in flow during other seasons. The Mann–Kendal Z-values for the flow in months January through June are all 2.63 for scenarios S1, S2, and S3. However, for scenario S2, the flow exhibits the highest relative increase compared to historical periods, with a growth of 40%. Scenario S2 shows the most significant increase, with May exhibiting the most noticeable increase. Scenario S3 shows the largest changes in May and November, with a 121% increase compared to the historical period in May and a 30% decrease in November.

Under the SSP5–8.5 climate scenario, scenarios S2 and S3 show a decrease in flow during the autumn compared to the historical period, while all other seasons show an increase in flow. Scenario S1 only shows an increase in flow during the spring season, with a decrease in flow during all other seasons. The Mann–Kendal Z-values for the flow in months January through June for scenarios S1, S2, and S3 are 2.25, 2.63, and 2.63, respectively. However, for scenario S2, the flow exhibits the highest relative increase compared to historical periods, with a growth of 46%. Scenario S2 shows the most significant increase, with April exhibiting the most noticeable increase. Scenario S3 shows the largest changes in March and November, with a 130% increase compared to the historical period in March and a 33% decrease in November. These months show a higher level of flow variability and require special attention compared to other months.

Except for scenario S1 under the SSP5–8.5 climate scenario (Mann–Kendal Z-value is the minimum among the nine scenarios, at 2.25), the differences between seasons for the other scenarios become more significant, and the hydrological process lines become steeper, indicating a more uneven distribution of flow throughout the year in the SRYR in the future. Except for scenario S1 under the SSP2–4.5 climate scenario, the peak flow for the future is expected to shift from July to June, indicating a lengthening of the flood season and an increase in the frequency of flood disasters occurring during the summer in the SRYR.

4. Conclusions

In the source region of the Yellow River (SRYR) from 2020 to 2099, there is a noticeable improvement in grassland growth status, indicating an overall positive trend in grassland development. Climatically, there is a clear increasing trend in temperature, precipitation, and longwave radiation, while wind speed shows a significant decreasing trend.

The probability of flood occurrences in the SRYR during the future period from 2020 to 2099 shows an increasing trend. However, the magnitude of this increase gradually diminishes over time, exhibiting a long-term declining trend. Overall, both land use and cover change (LUCC) and climate variability contribute to an increase in the multi-year average streamflow in the SRYR from 2020 to 2099. Specifically, under the SSP1–2.6, SSP2–4.5, and SSP5–8.5 scenarios, the streamflow increases by 48.8%, 24.5%, and 18.9%, respectively. The intensity of flood occurrences is greatest in the future under the SSP1–2.6 scenario, while it is minimal under the SSP5–8.5 scenario. However, there is greater fluctuation in the trend of streamflow variation under the latter scenario. Furthermore, under the SSP1–2.6 scenario, the increase in streamflow during the near future period (2020–2059) is greater than in the distant future (2059–2099). In contrast, for the SSP2–4.5 and SSP5–8.5 scenarios, the increase in streamflow during the near future period is greater than that during the distant future period.

Except for the S1_SSP5–8.5 scenario, the seasonal differences in other scenarios have increased, and the intra-annual hydrological processes have become steeper, indicating a more uneven distribution of streamflow in the SRYR in the future. With the exception of the S1_SSP2–4.5 scenario, where the peak flow occurs in September, in other scenarios, the future peak flows are expected to shift from July to June. This suggests that the flood season in the SRYR will extend in the future, leading to an increased frequency of flood occurrences during the summer. For future flow prediction research in the SRYR, more additional model data can be used to maximize simulation accuracy. Alternatively, a more comprehensive analysis of hydrological processes in the SRYR can be conducted from perspectives such as evapotranspiration and soil moisture.

Author Contributions: Conceptualization, Q.Z.; methodology, J.Z., L.W., D.Y., M.X. and Q.Z.; software, H.Z.; data curation, Q.Z.; writing—original draft preparation, H.Z.; writing—review and editing, H.Z. All authors have read and agreed to the published version of the manuscript.

Funding: This research was funded by the National Natural Science Foundation of China (No. U2243203; 42041005) and the Second Tibetan Plateau Scientific Expedition (No. 2019QZKK0304-02).

Data Availability Statement: Due to the data policies of data agencies in China, the meteorological data and streamflow data used in this research cannot be made publicly available. Other data can be downloaded from the corresponding websites marked in the text.

Conflicts of Interest: The authors declare no conflicts of interest.

References

1. Yang, K.; Dong, Y. Research on restricting factors and countermeasures of ecological protection and high-quality development of Yellow River basin—Analysis based on the multi-dimensional framework of "element-space-time". *J. Hydraul. Eng.* **2020**, *51*, 1038–1047.
2. Li, G. The speech of Li Guoying at 2022 National Working Conference on Water Resources. *China Water Resour.* **2022**, *2*, 1–10.
3. Zhang, J.; Cao, Z.; Jin, X.; Li, C. Research on comprehensive evaluation of the development quality of the Yellow River Basin. *J. Hydraul. Eng.* **2021**, *52*, 917–926.
4. Wang, Y.; Chen, Y.; Wang, H.; Lv, Y.; Hao, Y.; Cui, X.; Wang, Y.; Hu, R.; Xue, K.; Fu, B. Ecosystem Change and Its Ecohydrological Effect in the Yellow River Basin. *Bull. Natl. Nat. Sci. Found. China* **2021**, *35*, 520–528.
5. Wang, T.; Yang, H.; Yang, D.; Qin, Y.; Wang, Y. Quantifying the streamflow response to frozen ground degradation in the source region of the Yellow River within the Budyko framework. *J. Hydrol.* **2018**, *558*, 301–313. [CrossRef]
6. Wang, L.; Zhu, Q.A.; Zhang, J.; Liu, J.; Zhu, C.F.; Qu, L.S. Vegetation dynamics alter the hydrological interconnections between upper and mid-lower reaches of the Yellow River Basin, China. *Ecol. Indic.* **2023**, *148*, 110083. [CrossRef]
7. He, X.; Liang, J.; Zeng, G.; Yuan, Y.; Li, X. The Effects of Interaction between Climate Change and Land-Use/Cover Change on Biodiversity-Related Ecosystem Services. *Glob. Chall.* **2019**, *3*, 1800095. [CrossRef]
8. Cuo, L.; Lettenmaier, D.P.; Alberti, M.; Richey, J.E. Effects of a Century of Land Cover and Climate Change on the Hydrology of the Puget Sound Basin. *Hydrol. Process.* **2009**, *23*, 907–933. [CrossRef]

9. Ning, J.; Liu, J.; Kuang, W.; Xu, X.; Zhang, S.; Yan, C.; Li, R.; Wu, S.; Hu, Y.; Du, G.; et al. Spatiotemporal patterns and characteristics of land-use change in China during 2010–2015. *J. Geogr. Sci.* **2018**, *28*, 547–562. [CrossRef]
10. Zhou, G.; Wei, X.; Chen, X.; Zhou, P.; Liu, X.; Xiao, Y.; Sun, G.; Scott, D.F.; Zhou, S.; Han, L.; et al. Global pattern for the effect of climate and land cover on water yield. *Nat. Commun.* **2015**, *6*, 40. [CrossRef]
11. Yang, W.; Long, D.; Bai, P. Impacts of future land cover and climate changes on runoff in the mostly afforested river basin in North China. *J. Hydrol.* **2019**, *570*, 201–219. [CrossRef]
12. Chen, L.; Liu, C. Influence of climate and land-cover change on runoff of the source regions of Yellow River. *China Environ. Sci.* **2007**, *27*, 559–565.
13. Thanapakpawin, P.; Richey, J.; Thomas, D.; Rodda, S.; Campbell, B.; Logsdon, M. Effects of landuse change on the hydrologic regime of the Mae Chaem river basin, NW Thailand. *J. Hydrol.* **2007**, *334*, 215–230. [CrossRef]
14. Hilker, T.; Natsagdorj, E.; Waring, R.H.; Lyapustin, A.; Wang, Y. Satellite observed widespread decline in Mongolian grasslands largely due to overgrazing. *Glob. Chang. Biol.* **2014**, *20*, 418–428. [CrossRef]
15. Zhu, Q.; Chen, H.; Peng, C.; Liu, J.; Piao, S.; He, J.-S.; Wang, S.; Zhao, X.; Zhang, J.; Fang, X.; et al. An early warning signal for grassland degradation on the Qinghai-Tibetan Plateau. *Nat. Commun.* **2023**, *14*, 6406. [CrossRef]
16. Jaramillo, F.; Prieto, C.; Lyon, S.W.; Destouni, G. Multimethod assessment of evapotranspiration shifts due to non-irrigated agricultural development in Sweden. *J. Hydrol.* **2013**, *484*, 55–62. [CrossRef]
17. Zuo, Q.; Ding, X.; Cui, G.; Zhang, W. Yellow River Basin Management under Pressure: Present State, Restoration and Protection II: Lessons from a Special Issue. *Water* **2024**, *16*, 999. [CrossRef]
18. Yi, D. Simulation and Analysis of Runoff in the Source Region of the Yellow River Based on CMIP6 Climate Model. Master's Thesis, Northwest A&F University, Xianyang, China, 2022.
19. Liu, Y.; Su, Y.; Wang, L.; Zhao, Y. Simulation and Evaluation of Runoff in Tributary of Weihe River Basin in Western China. *Water* **2024**, *16*, 221. [CrossRef]
20. Yan, Y. Simulation of Water Resources in the Upper Reaches of the Yellow River and Its Future Evolution. Master's Thesis, East China Normal University, Shanghai, China, 2017.
21. Jia, H.; Li, X.; Wen, J.; Chen, Y. Runoff change simulation and future trend projection in the source area of the Yellow River. *Resour. Sci.* **2022**, *44*, 1292–1304. [CrossRef]
22. Chawla, I.; Mujumdar, P.P. Isolating the impacts of land use and climate change on streamflow. *Hydrol. Earth Syst. Sci.* **2015**, *19*, 3633–3651. [CrossRef]
23. Wei, J.; Chang, J.; Chen, L. Runoff change in upper reach of Yellow River under future climate change based on VIC model. *J. Hydroelectr. Eng.* **2016**, *35*, 65–74.
24. Han, Q.; Xue, L.; Qi, T.; Liu, Y.; Yang, M.; Chu, X.; Liu, S. Assessing the Impacts of Future Climate and Land-Use Changes on Streamflow under Multiple Scenarios: A Case Study of the Upper Reaches of the Tarim River in Northwest China. *Water* **2024**, *16*, 100. [CrossRef]
25. Zhu, T. Attribution Analysis of Runoff Change in the YellowRiver Basin under Climate Model. Master's Thesis, Zhengzhou University, Zhengzhou, China, 2022.
26. He, S.; Chen, K.; Liu, Z.; Deng, L. Exploring the impacts of climate change and human activities on future runoff variations at the seasonal scale. *J. Hydrol.* **2023**, *619*, 129382. [CrossRef]
27. Beven, K.; Freer, J. Equifinality, data assimilation, and uncertainty estimation in mechanistic modelling of complex environmental systems using the GLUE methodology. *J. Hydrol.* **2001**, *249*, 11–29. [CrossRef]
28. Wang, Z.; Tang, Q.; Wang, D.; Xiao, P.; Xia, R.; Sun, P.; Feng, F.X. Attributing trend in naturalized streamflow to temporally explicit vegetation change and climate variation in the Yellow River basin of China. *Hydrol. Earth Syst. Sci.* **2022**, *26*, 5291–5314. [CrossRef]
29. Wang, M. Precipitation Runoff Trend in the Source Region of the Yellow River under Future Climate Change. Master's Thesis, Qinghai University, Xining, China, 2019.
30. Ji, G.; Lai, Z.; Xia, H.; Liu, H.; Wang, Z. Future Runoff Variation and Flood Disaster Prediction of the Yellow River Basin Based on CA-Markov and SWAT. *Land* **2021**, *10*, 421. [CrossRef]
31. Yang, X.; Zhou, B.; Xu, Y.; Han, Z. CMIP6 Evaluation and Projection of Temperature and Precipitation over China. *Adv. Atmos. Sci.* **2021**, *38*, 817–830. [CrossRef]
32. Zhou, T.; Zou, L.; Chen, X. Commentary on the Coupled Model Intercomparison Project Phase 6 (CMIP6). *Progress. Inquis. Mutat. Clim.* **2019**, *15*, 445–456.
33. Zhang, L.; Chen, X.; Xin, X. Short commentary on CMIP6 Scenario Model Intercomparison Project (ScenarioMIP). *Progress. Inquis. Mutat. Clim.* **2019**, *15*, 519–525.
34. Wang, J.; Liu, S.; Hao, Y.; Tang, J. Change trend of runoff in source region of Yellow River under A1B scenario. *J. Hohai Univ. Nat. Sci.* **2014**, *42*, 95–100.
35. Zhao, F.; Xu, Z. Comparative analysis on downscaled climate scenarios for headwater catchment of Yellow River using SDS and Delta methods. *Acta Meteorol. Sin.* **2007**, *65*, 653–662.
36. Zhao, M.; Su, B.; Jiang, T.; Wang, A.; Tao, H. Simulation and Projection of Precipitation in the Upper Yellow River Basin by CMIP6 Multi-Model Ensemble. *Plateau Meteorol.* **2021**, *40*, 547–558.
37. Alaniz, A.J.; Smith-Ramirez, C.; Rendon-Funes, A.; Hidalgo-Corrotea, C.; Carvajal, M.A.; Vergara, P.M.; Fuentes, N. Multiscale spatial analysis of headwater vulnerability in South-Central Chile reveals a high threat due to deforestation and climate change. *Sci. Total Environ.* **2022**, *849*, 157930. [CrossRef]

38. Martínez-Retureta, R.; Aguayo, M.; Abreu, N.J.; Urrutia, R.; Echeverría, C.; Lagos, O.; Rodríguez-López, L.; Duran-Llacer, I.; Barra, R.O. Influence of Climate and Land Cover/Use Change on Water Balance: An Approach to Individual and Combined Effects. *Water* **2022**, *14*, 2304. [CrossRef]
39. Pham Thi Thao, N.; Dao Nguyen, K.; Nguyen Thi Thuy, T.; Tran Van, T.; Fang, S. Hydrological impacts of future climate and land use/cover changes in the Lower Mekong Basin: A case study of the Srepok River Basin, Vietnam. *Environ. Monit. Assess.* **2022**, *194* (Suppl. S2), 768.
40. Si, J.; Li, J.; Lu, S.; Qi, X.; Zhang, X.; Bao, W.; Zhang, X.; Zhou, S.; Jin, C.; Qi, L.; et al. Effects of Climate Change on Surface Runoff and Soil Moisture in the Source Region of the Yellow River. *Water* **2023**, *15*, 2104. [CrossRef]
41. Joseph, J.; Ghosh, S.; Pathak, A.; Sahai, A.K. Hydrologic impacts of climate change: Comparisons between hydrological parameter uncertainty and climate model uncertainty. *J. Hydrol.* **2018**, *566*, 1–22. [CrossRef]
42. Wilby, R.L.; Harris, I. A framework for assessing uncertainties in climate change impacts: Low-flow scenarios for the River Thames, UK. *Water Resour. Res.* **2006**, *42*, W02419. [CrossRef]
43. Zhang, H.; Huang, G.H.; Wang, D.; Zhang, X. Uncertainty assessment of climate change impacts on the hydrology of small prairie wetlands. *J. Hydrol.* **2011**, *396*, 94–103. [CrossRef]
44. Trolle, D.; Nielsen, A.; Andersen, H.E.; Thodsen, H.; Olesen, J.E.; Borgesen, C.D.; Refsgaard, J.C.; Sonnenborg, T.O.; Karisson, I.B.; Christensen, J.P.; et al. Effects of changes in land use and climate on aquatic ecosystems: Coupling of models and decomposition of uncertainties. *Sci. Total Environ.* **2019**, *657*, 627–633. [CrossRef]
45. Mainali, S.; Sharma, S. Climate Change Effects on Rainfall Intensity-Duration-Frequency (IDF) Curves for the Lake Erie Coast Using Various Climate Models. *Water* **2023**, *15*, 4063. [CrossRef]
46. Yutong, Z.; Yuefei, H.; Sha, Z.; Keyi, W.; Guangqian, W. Effect partition of climate and catchment changes on runoff variation at the headwater region of the Yellow River based on the Budyko complementary relationship. *Sci. Total Environ.* **2018**, *643*, 1166–1177.
47. Xu, Y.; Yu, L.; Peng, D.; Zhao, J.; Cheng, Y.; Liu, X.; Li, W.; Meng, R.; Xu, X.; Gong, P. Annual 30-m land use/land cover maps of China for 1980-2015 from the integration of AVHRR, MODIS and Landsat data using the BFAST algorithm. *Sci. China-Earth Sci.* **2020**, *63*, 1390–1407. [CrossRef]
48. Allen, R.G.; Pereira, L.S.; Raes, D.; Smith, M. *Crop Evapotranspiration: Guidelines for Computing Crop Water Requirements*; Irrigation and Drainage Paper No 56; Food and Agriculture Organization of the United Nations (FAO): Rome, Italy, 1998.
49. Maidment, D.R. *Handbook of Hydrology*; Science Press: New York, NY, USA, 2008.
50. Liao, W.; Liu, X.; Xu, X.; Chen, G.; Liang, X.; Zhang, H.; Li, X. Projections of land use changes under the plant functional type classification in different SSP-RCP scenarios in China. *Sci. Bull.* **2020**, *65*, 1935–1947. [CrossRef]
51. Fang, G.H.; Yang, J.; Chen, Y.N.; Zammit, C. Comparing bias correction methods in downscaling meteorological variables for a hydrologic impact study in an arid area in China. *Hydrol. Earth Syst. Sci.* **2015**, *19*, 2547–2559. [CrossRef]
52. M'Po, Y.N.T.; Lawin, A.E.; Oyerinde, G.T.; Yao, B.K.; Afouda, A.A. Comparison of Daily Precipitation Bias Correction Methods Based on Four Regional Climate Model Outputs in Ouémé Basin, Benin. *Hydrology* **2017**, *4*, 58–71. [CrossRef]
53. Mahmood, R.; Jia, S.; Tripathi, N.K.; Shrestha, S. Precipitation Extended Linear Scaling Method for Correcting GCM Precipitation and Its Evaluation and Implication in the Transboundary Jhelum River Basin. *Atmosphere* **2018**, *9*, 160. [CrossRef]
54. Zhang, L. Hydrological Simulations and Scenario Analyses in the Upper Heihe River Basin Using the DHSVM and SWAT Models. Ph.D. Thesis, University of Chinese Academy of Sciences, Beijing, China, 2017.
55. Zhao, Y. Research on the Distributed Model Simulation of theSpatial/ Temporal Hydrological Characteristics in a Cold Alpine Basin. Master's Thesis, Nanjing Normal University, Nanjing, China, 2019.
56. Luz; Adriana; Cuartas; Javier; Tomasella; Antonio; Donato; Nobre; Carlos; Afonso, Distributed hydrological modeling of a micro-scale rainforest watershed in Amazonia: Model evaluation and advances in calibration using the new HAND terrain model. *J. Hydrol.* **2012**, *462–463*, 15–27.
57. Cuo, L.; Giambelluca, T.W.; Ziegler, A.D. Lumped parameter sensitivity analysis of a distributed hydrological model within tropical and temperate catchments. *Hydrol. Process.* **2011**, *25*, 2405–2421. [CrossRef]
58. Moriasi, D.N.; Arnold, J.G.; Liew, M.W.V.; Bingner, R.L.; Harmel, R.D.; Veith, T.L. Model Evaluation Guidelines for Systematic Quantification of Accuracy in Watershed Simulations. *Trans. ASABE* **2007**, *50*, 885–900. [CrossRef]
59. Mann, H.B. Nonparametric test against trend. *Econometrica* **1945**, *13*, 245–259. [CrossRef]
60. Kendall, M.G. Rank Correlation Methods. *Br. J. Psychol.* **1990**, *25*, 86–91. [CrossRef]
61. Farlie, D.J.G. Rank Correlation Methods. *J. R. Stat. Soc. Ser. A* **1971**, *134*, 682. [CrossRef]
62. Li, B.; Shi, X.; Lian, L.; Chen, Y.; Chen, Z.; Sun, X. Quantifying the effects of climate variability, direct and indirect land use change, and human activities on runoff. *J. Hydrol.* **2020**, *584*, 124684. [CrossRef]
63. Soltani, M.; Laux, P.; Kunstmann, H.; Stan, K.; Sohrabi, M.M.; Molanejad, M.; Sabziparvar, A.A.; Saadatabadi, A.R.; Ranjbar, F.; Rousta, I. Assessment of climate variations in temperature and precipitation extreme events over Iran. *Theor. Appl. Climatol.* **2015**, *126*, 775–795. [CrossRef]